GDCh Research Article Angewandte International Edition www.angewandte.org

Check for updates

How to cite: *Angew. Chem. Int. Ed.* **2025**, *64*, e202504212
doi.org/10.1002/anie.202504212

Oxygen Evolution Reaction | Hot Paper

Leaching-Induced Ti Trapping Stabilizes Amorphous IrO_x for Proton Exchange Membrane Water Electrolysis

Hao Yang Lin, Wen Jing Li, Miao Yu Lin, Hao Guan Xu, Song Ru Fang, Yao Lv, Wenbo Li, Jianwei Guo, Huai Qin Fu, Hai Yang Yuan, Chenghua Sun, Sheng Dai, Peng Fei Liu,* and Hua Gui Yang**

Abstract: Transition metal nitrides are promising conductive support materials in oxygen evolution reaction (OER), whereas it is unclear if their electrochemical oxidation during prolonged test would affect the OER catalysts. Herein, we demonstrate that the leaching-induced Ti trapping effect from TiN supports effectively stabilizes the electrochemically oxidized amorphous IrO_x catalyst. Structural characterizations reveal that the TiN support experiences severe leaching during OER test, leaving minor amounts of Ti–O species trapping on IrO_x clusters, which mitigate the overoxidation of Ir(III) species and elongate the Ir–O bonds. This leads to 70% reduction of lattice oxygen oxidation and the substantially reduced Ir leaching. Additionally, self-thickening of the catalyst layers is found during proton exchange membrane water electrolysis (PEMWE), enabling an ultralow catalyst loading of 87 μg_{Ir} cm^{-2} to obtain a stable operation at 1.0 A cm^{-2} for 500 h. This work deepens the understanding of TiN-supported catalysts for long-term stable OER electrocatalysis.

Introduction

Proton exchange membrane water electrolysis (PEMWE) technology is becoming a crucial role in renewable energy conversion and storage, with the energy efficiency as the key to its practical application.[1–3] However, the sluggish kinetics of the four-electron-transferred oxygen evolution reaction (OER) have restricted the overall efficiency of water splitting.[4,5] Currently, iridium-based oxides, serving as the benchmark catalysts for OER, are highly relied upon, whereas their limited resource becomes a bottleneck to the increasing demand of electrolytic hydrogen.[6,7]

At present, there are two effective strategies to reduce iridium loading amount: 1) enhancing the intrinsic activity of Ir-based catalysts, for instance, by creating nanostructured hierarchical and porous iridium oxides with ultrafine grains and rich inter-granular boundaries,[8–10] which enables the PEMWE to operate at high current densities (>1.0 A cm^{-2}) and thereby reduces the electrode surface area and the overall Ir usage; and 2) dispersing low-loading iridium oxides on suitable support materials to meet the demand for sufficient thickness, homogeneous composition, and structural integrity of the catalyst layers, meanwhile reducing the overall Ir content without sacrificing the in-plane conductivity and structural mechanical stability of the electrode.[11–14] However, some practical issues should be noted. The nanosized iridium oxides, whether are supported or not, are usually accompanied by complex grain boundaries, lattice dislocations, and defects, which are more active but prone to suffer from Ir dissolution on the disordered surface than the highly crystalline rutile IrO_2 during OER process.[15–17] Moreover, the widely used corrosion-resistant transition metal oxide (e.g., Ti, Nb, W-contained oxides) support materials exhibit rather poor conductivity relative to precious metal oxides, and therefore usually necessitate high loading of iridium oxides to ensure sufficient interfacial contact and electron transfer between the catalyst layers and porous transport layers (PTLs) in practical PEMWE.

Recent studies have revealed promising potential of transition metal nitrides as support materials for electrocatalysts,[18–20] among which TiN has received increasing attention for its metal-like conductivity.[21–25] But in fact, these metal nitrides undergo gradual oxidation in OER conditions. Previous researches were generally based

[*] H. Y. Lin, W. J. Li, M. Y. Lin, H. G. Xu, S. R. Fang, J. Guo, H. Y. Yuan, P. F. Liu, H. G. Yang
Key Laboratory for Ultrafine Materials of Ministry of Education, Shanghai Engineering Research Center of Hierarchical Nanomaterials, School of Materials Science and Engineering, East China University of Science and Technology, 130 Meilong Road, Shanghai 200237, China
E-mail: pfliu@ecust.edu.cn
hgyang@ecust.edu.cn

Y. Lv, W. Li, S. Dai
Key Laboratory for Advanced Materials and Feringa Nobel Prize Scientist Joint Research Center, Institute of Fine Chemicals, School of Chemistry and Molecular Engineering, East China University of Science and Technology, 130 Meilong Road, Shanghai 200237, China
E-mail: shengdai@ecust.edu.cn

H. Q. Fu
Centre for Catalysis and Clean Energy, Gold Coast Campus, Griffith University, Gold Coast, QLD 4222, Australia

C. Sun
Department of Chemistry and Biotechnology, Faculty of Science, Engineering and Technology, Swinburne University of Technology, Hawthorn 3122, Australia

Additional supporting information can be found online in the Supporting Information section

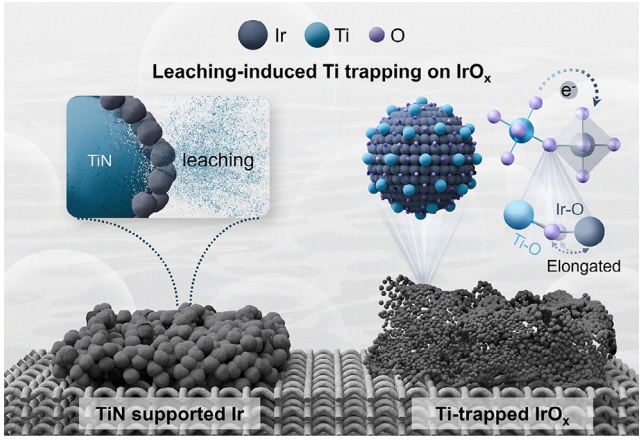

Scheme 1. Ti leaching from TiN support induces a trapping effect in stabilizing amorphous IrO_x during OER. The pristine Ir/TiN undergoes gradual Ti leaching under strong oxidative OER conditions. The Ti leaching process is accompanied with Ti trapping on the surface of IrO_x, leading to mitigated overoxidation of Ir(III) species and the elongated Ir—O bonds. It aids to significantly suppress lattice oxygen oxidation and the relevant Ir(III) leaching, thereby effectively stabilizing the amorphous IrO_x. The severe Ti leaching also results in nanoporous agglomerates of IrO_x clusters, causing self-thickening of the catalyst layer, which benefit to the high-performance PEMWE with ultrathin catalyst coatings.

on a conventional understanding that passive transition metal oxide films would be formed on the metal nitride surface and act as protective layers against further corrosion, which was verified as electrochemically stable in fuel cell conditions.[19,20,26] However, when exposed to much more oxidizing OER potentials during long-term operations, it remains unclear if the partially or even fully oxidized metal nitride support would influence the catalyst active centers. This knowledge gap has impeded the accurate understanding of structure–performance relationships of the OER catalysts based on metal nitride support materials and additionally a further rational catalyst design.

Here, we start from the investigations on the response of electrochemical oxidation of bare TiN at OER potentials and demonstrate its evolution into fragmented hollow TiO_2 shells together with severe Ti leaching. Next, we load Ir on the TiN support (Ir/TiN) as a model catalyst to assess the influence of TiN degradation on the OER performance. The Ir/TiN catalyst initially exhibits an optimal OER activity compared to TiO_2 supported or unsupported iridium, with a mass activity even 74 times higher than the commercial IrO_2/TiO_2 (Umicore). Remarkably, the amorphous IrO_x electrochemically oxidized from Ir/TiN shows significantly improved OER stability with suppressed Ir leaching, compared to those TiO_2 supported or unsupported counterparts. It maintains stable operation for over 1000 h at 10 mA cm^{-2} with a decay rate of only 42 μV h^{-1}. Structural characterizations along with theoretical calculations reveal that the TiN leaching-induced Ti trapping on amorphous IrO_x mitigates the overoxidation of Ir(III) species and elongates Ir—O bonds, which aids to inhibit the lattice oxygen from oxidation, thus effectively stabilizing the amorphous IrO_x (Scheme 1). The gradual leaching of the TiN support from Ir/TiN during oxidization also results in the formation of much more nanoporous agglomerates of IrO_x clusters, contributing to self-thickening of the catalyst layers during operation of PEMWE. This allows for an electrode architecture featuring ultrathin catalyst layers without sacrificing structural integrity or interfacial contact. Consequently, the resulting PEMWE using the Ir/TiN anode catalyst, with an ultralow loading of 87 μg_{Ir} cm^{-2}, achieves low voltages of 1.60 and 1.80 V at 1.0 and 2.0 A cm^{-2}, respectively, while maintaining stable operation at 1.0 A cm^{-2} for 500 h. This work unveils the structural evolution of TiN support for OER catalysts and emphasizes its leaching-induced Ti trapping effect in stabilizing the active amorphous iridium oxides compared to the conventional stable support materials.

Results and Discussion

Characterizations of Electrochemically Oxidized TiN

To evaluate the corrosion resistance of TiN as the support material for acidic OER, first it was immersed in 0.5 M H_2SO_4 for 24 h. The inductively coupled plasma optical emission spectroscopy (ICP-OES) result showed 2.9% Ti leached out in the acidic solution. Then the prepared carbon paper electrode sprayed with TiN was applied as the anode under a potentiostatic test at 1.6 V versus the reversible hydrogen electrode (versus RHE) for 100 h (denoted as TiN-derived TiO_2) (Figure S1a). Different from the conventional understanding that the bulk TiN could be well retained except slight surface oxidation, it was found 54% Ti species leached from TiN into the electrolyte (Figure S1b). The Ti leaching would be more severe at high OER current densities (e.g., in the case of Ir loading on TiN) as the Ti species are prone to diffuse into the electrolyte before being oxidized to TiO_2 for the collapse and detachment of oxygen bubbles from the catalyst surface.[27] It was also consistent with the X-ray diffraction (XRD) patterns (Figure 1a) that the diffraction peaks of pristine TiN disappeared after electrochemical oxidization. The transmission electron microscopy (TEM) images of TiN-derived TiO_2 exhibited a weak contrast, as compared to the pristine TiN particles (Figure 1b), revealing only flocculent and fragmented hollow shells were retained. High resolution TEM (HRTEM) images and the corresponding fast Fourier transform (FFT) patterns (Figure 1c,d) further demonstrated the evolution of TiN particles into TiO_2 fragments, which was consistent with the energy-dispersive X-ray spectroscopy (EDS) elemental maps (Figure 1e). In addition, electron energy loss spectroscopy (EELS) was applied to investigate the variations of electronic structure (Figure 1f). First, N signals disappeared in the TiN-derived TiO_2 spectrum, whereas O signals were observed, indicating the transformation from metal nitrides to oxides. It agreed with the EDS elemental analyses, as shown in Figure 1g. Second, Ti-$L_{2,3}$ edges of TiN-derived TiO_2 (Figure 1f) were double split similarly to the most Ti(IV) compounds[28] and shifted toward higher energy region compared with the pristine TiN, suggesting an increased valence state of Ti.[29] On the basis of these results, next, Ir clusters were loaded on TiN support to study

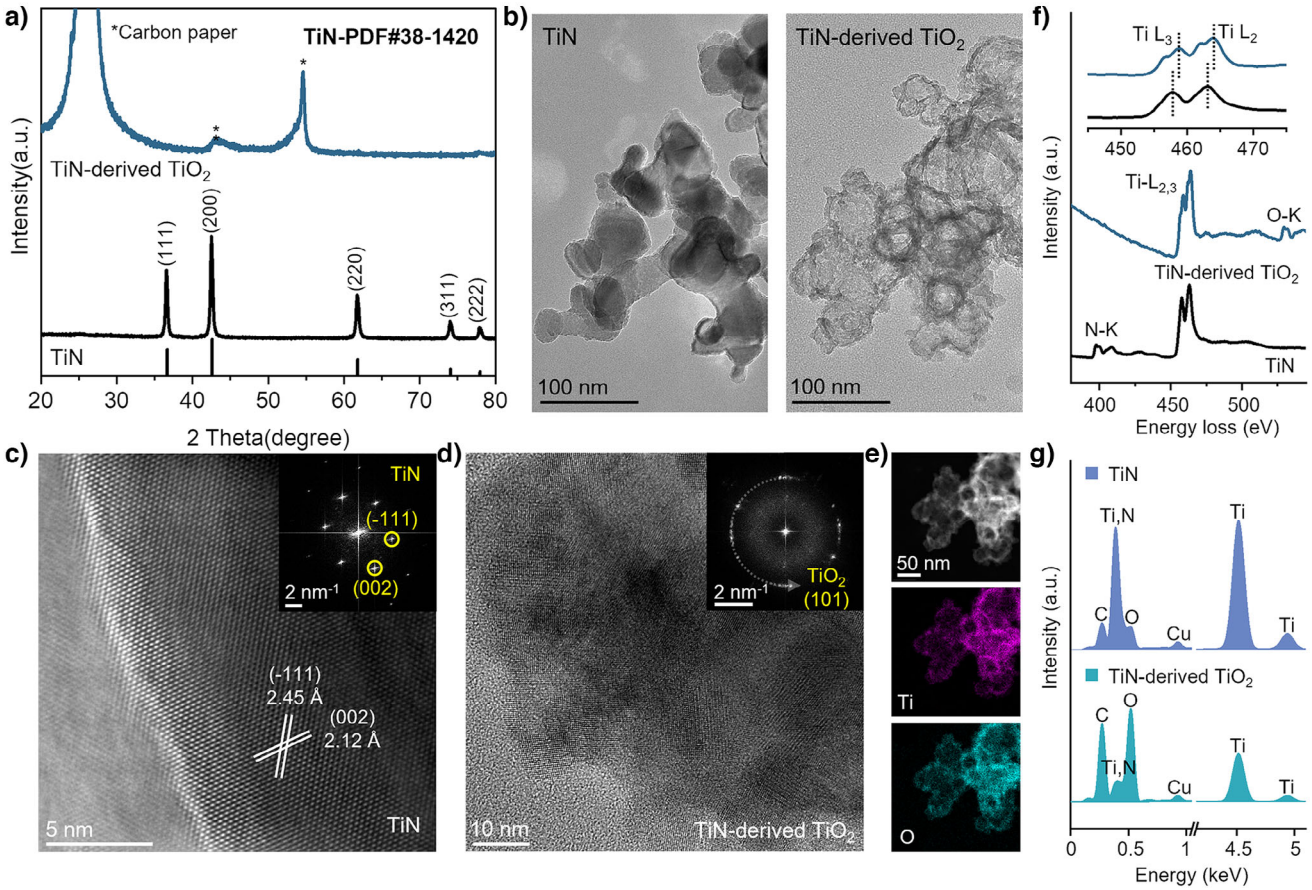

Figure 1. Structural characterizations of bare TiN support before and after electrochemical oxidization. a) XRD patterns of pristine TiN and TiN after 100 h at 1.6 V (denoted as TiN-derived TiO_2). b) TEM images of TiN and TiN-derived TiO_2. c) HRTEM image of TiN. Inset is the corresponding FFT pattern. d) HRTEM image of TiN-derived TiO_2. Inset is the corresponding FFT pattern. e) HAADF-STEM and the corresponding EDS elemental maps of TiN-derived TiO_2. f) EELS results of TiN and TiN-derived TiO_2. g) EDS elemental analyses of TiN and TiN-derived TiO_2. C and Cu signals were from the Cu grids of the TEM samples.

how the TiN leaching-induced Ti trapping would affect the electrochemically oxidized amorphous IrO_x.

Synthesis and Characterization of Ir/TiN

The xIr/TiN samples were prepared with different H_2IrCl_6 feeding (x = 0.1, 0.2, 0.3, and 0.4, corresponding to x mmol feeding of H_2IrCl_6) by an ethylene glycol (EG) reduction method. TiO_2 supported Ir (Ir/TiO_2) and Ir black without support (Ir-EG) were also prepared as comparisons. Considering its best OER performance, 0.3Ir/TiN was focused on the study and marked as Ir/TiN for simplicity. The XRD patterns (Figure S2) showed that the diffraction peaks of TiN supports dominate the XRD patterns of Ir/TiN with different Ir loadings. Broadened peaks at ~41° can be ascribed to the Ir clusters with small grain size supported on TiN. High-angle annular dark field-scanning transmission electron microscopy (HAADF-STEM) image (Figure 2a) evidenced that Ir clusters with an average size of 1.5 nm (Figure 2b) were highly dispersed on the surface of TiN. EDS elemental analyses (Figure 2c and Table S1) further exhibited the Ir clusters on TiN with a 30.5 wt% content of Ir, well consistent with the ICP-OES result (31 wt%). The FFT pattern (Figure 2d) derived from the selected area in Figure 2a also demonstrated the phases of Ir and TiN, respectively. Atomic-resolution HAADF-STEM image (Figure 2e) and the 3D surface plot (Figure S3) further showed the Ir cluster on TiN, highlighting the interaction between Ir and Ti atoms at the interface. Characterizations on Ir/TiO_2 and Ir-EG were also conducted through XRD, TEM, and EDS, verifying their successful synthesis (Figures S4–S6).

Then X-ray absorption fine structure (XAFS) and X-ray photoelectron spectroscopy (XPS) were employed to examine the chemical state and coordination environment of Ir/TiN. The Ir valence state can be compared from the Ir L_3-edge white line position determined by the minimum of the second derivative of X-ray absorption near-edge structure (XANES) spectra (Figure 2f).[30,31] It showed that the white line position of Ir/TiN was between that of Ir foil and IrO_2, suggesting the mixture of metallic and oxidized Ir species, consistent with the Ir 4f XPS results (Figure S7). Moreover, the positive shift of the white line position for Ir/TiN and Ir/TiO_2 compared with the unsupported Ir-EG indicated their increased Ir oxidation states, implying the possible electronic interaction between the Ir-anchored support interface.[21] Extended X-ray

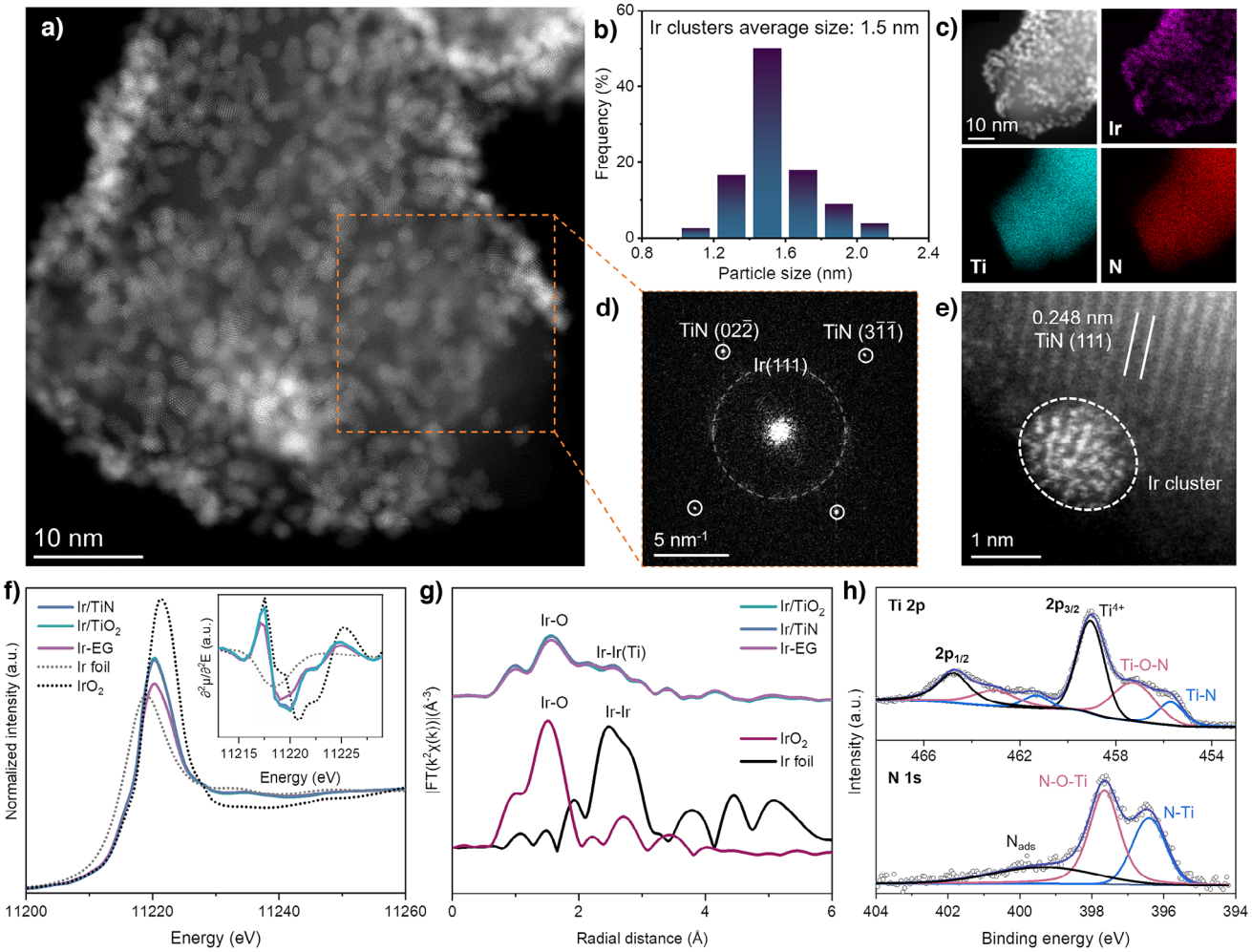

Figure 2. Structural characterizations of pristine Ir/TiN catalyst. a) HAADF-STEM image of Ir/TiN. b) Cluster size distribution of Ir clusters on Ir/TiN. c) HAADF-STEM image and the corresponding EDS elemental maps of Ir/TiN. d) FFT pattern of the orange square area in (a). e) Atomic-scale HAADF-STEM image of Ir/TiN. f) Normalized Ir L_3-edge XANES spectra of Ir/TiN, Ir/TiO_2, Ir-EG, Ir foil, and IrO_2. Inset shows the corresponding second derivative curves. g) Fourier-transforms of k^2-weight Ir L_3-edge EXAFS spectra of Ir/TiN, Ir/TiO_2, Ir-EG, IrO_2, and Ir foil. h) XPS spectra of Ti 2p and N 1s for Ir/TiN.

absorption fine structure (EXAFS) spectra (Figure 2g) and wavelet transformations (Figure S8) showed the coexistence of Ir–O and Ir–Ir(Ti) coordination in Ir/TiN,[32] corresponding to its mixed oxidation state. The Ti 2p and N 1s XPS spectra of Ir/TiN (Figure 2h) suggested the surface partially oxidized TiN support with Ti–O, Ti–O–N, and Ti–N species, which was probably due to the surface adsorbed oxygen species during catalyst preparation.[21,33]

Electrocatalytic Performance

The OER performance of Ir/TiN was evaluated in a typical three-electrode H-type cell separated by Nafion 117 membrane, with Ir/TiO_2, Ir-EG, commercial IrO_2 (Adamas-beta), and IrO_2/TiO_2 (Umicore) as comparisons. The samples were activated and stabilized by cyclic voltammetry (CV) before collecting polarization curves. First, the bare TiN was evidenced ineffective with almost no OER current response (Figure 3a). Then Ir/TiN catalyst prepared with different H_2IrCl_6 feeding were evaluated (Figures S9 and S10), among which 0.3Ir/TiN presented an optimal OER activity with an overpotential of 277 mV at 10 mA cm^{-2}. Deteriorative performance was obtained on 0.4Ir/TiN, probably owing to the agglomeration of Ir clusters under excessive loading and the resultant weakened Ir–Ti interaction in the interface. It also agreed with a relatively low OER activity (299 mV at 10 mA cm^{-2}) for the Ir-EG catalyst without Ir–Ti interaction. The activity of Ir/TiN also outperformed Ir/TiO_2 (296 mV at 10 mA cm^{-2}), demonstrating a more competitive role of TiN support. In addition, comparisons with commercial IrO_2 (Adamas-beta, 334 mV at 10 mA cm^{-2}) and IrO_2/TiO_2 (Umicore, 371 mV at 10 mA cm^{-2}) also indicated its excellent performance. Furthermore, much lower Tafel slope (Figure 3b) of 43 mV dec^{-1} corroborated the accelerated OER kinetics on Ir/TiN. It also manifested the highest mass activity of 1472 mA mg_{Ir}^{-1} for Ir/TiN at 1.58 V (Figures 3c and S11) and was 74 times higher than the commercial IrO_2/TiO_2

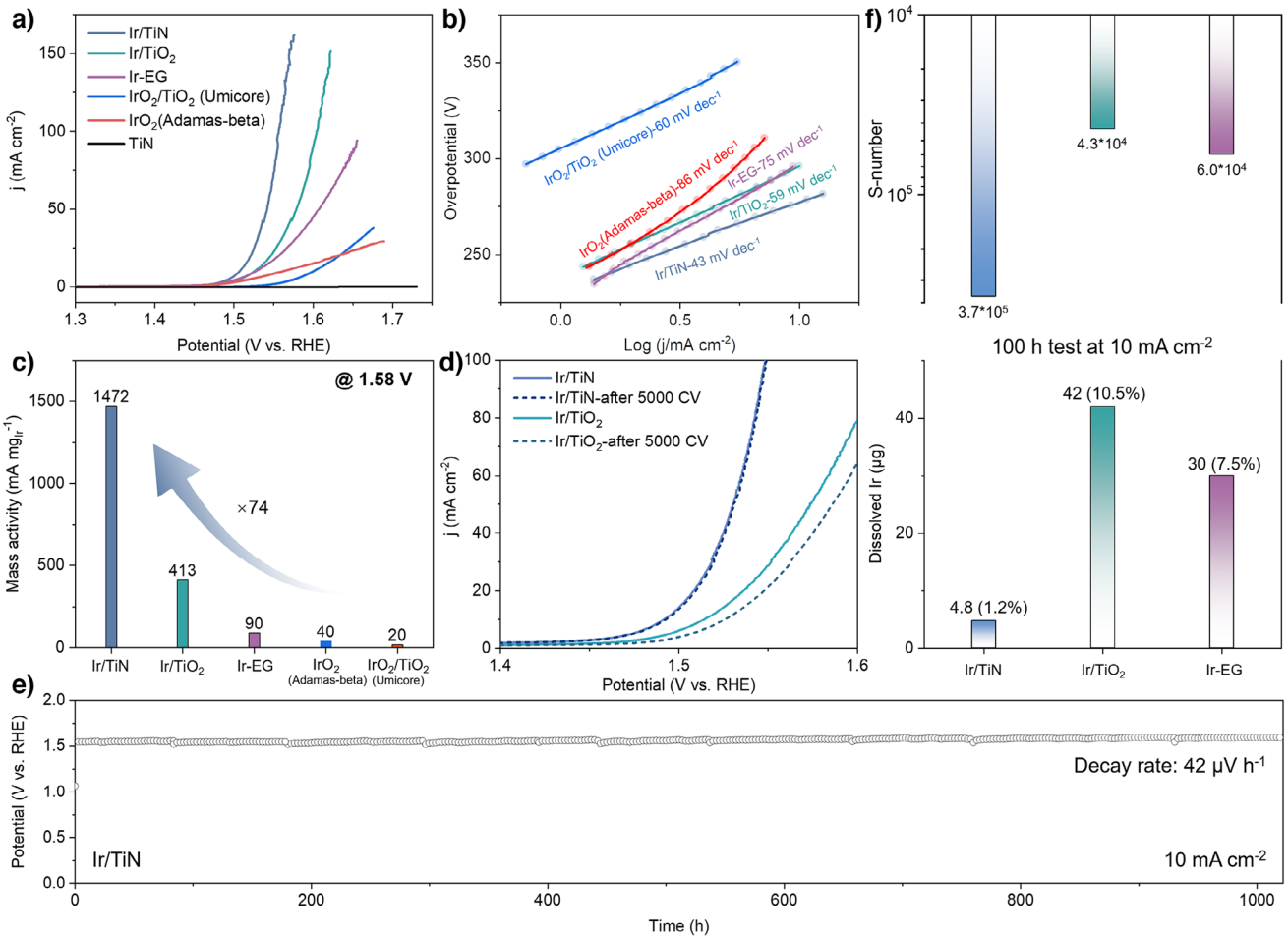

Figure 3. Electrocatalytic OER performance in three-electrode system. a) Representative LSV curves. b) Tafel plots derived from (a). c) Calculated mass activity at 1.58 V. d) OER polarization curves of Ir/TiN and Ir/TiO_2 before and after 5000 CV cycles. e) Long-term OER chronopotentiometry test for Ir/TiN at 10 mA cm^{-2}. f) Dissolved Ir after 100 h test at 10 mA cm^{-2} and the calculated S-number for Ir/TiN, Ir/TiO_2, and Ir-EG.

(Umicore). The specific activity normalized by electrochemical surface area (ECSA) was further estimated to reveal the intrinsic activity of Ir/TiN, which outperformed those of TiO_2-supported and unsupported Ir catalysts (Figure S12).

The OER durability was evaluated by CV and chronopotentiometry techniques. As shown in Figure 3d, Ir/TiN exhibited a robust stability and retained its initial activity after 5000 CV cycles. In contrast, Ir/TiO_2 showed a 22 mV increase of the potential. It can be also reflected from the potential degradations during chronopotentiometry tests at 10 mA cm^{-2}. Ir/TiN operated steadily during 1000 h test with a decay rate of only 42 μV h^{-1} (Figure 3e), much less than that of 220 and 250 μV h^{-1} for Ir-EG and Ir/TiO_2 catalysts (Figure S13), respectively. Additionally, Ir dissolutions in the electrolyte from the catalysts were further detected by ICP-OES after 100 h OER tests. Specifically, only 4.8 μg_{Ir} (i.e., 1.2% of Ir) dissolved from Ir/TiN (Figure 3f), which was reduced by 84% and 89% that of Ir-EG (30 μg_{Ir}) and Ir/TiO_2 (42 μg_{Ir}). The corresponding stability number (S-number) of Ir/TiN was calculated to be 3.7 × 10^5, 8.6 and 6.2 times that of Ir/TiO_2 and Ir-EG, indicating the prolonged lifetime of Ir/TiN.

Leaching-Induced Ti trapping Stabilized Amorphous IrO_x

Apart from the Ir dissolution during OER, much more intense Ti leaching was found from Ir/TiN (Figures S14–S16). There were 88% Ti species leached out into the electrolyte for the oxidized Ir/TiN catalyst (Ir/TiN after 100 h OER test at 10 mA cm^{-2}) evaluated by ICP-OES, which was also supported by the XRD results of the disappeared diffraction peaks of pristine TiN support (Figure S15). According to the EDS results, Ti/(Ti + Ir) atomic ratio for the Ir/TiN sample decreased from 85% in pristine to 74% after 24 h test, and it further decreased to 18% after 100 h test (Table S2). By contrast, negligible Ti dissolution was detected from oxidized Ir/TiO_2 (Ir/TiO_2 after 100 h OER test at 10 mA cm^{-2}), and the XRD and TEM characterizations confirmed the well maintained TiO_2 support (Figure S17), indicating the completely different role of TiN from TiO_2 support (Figure 4a). The dissolution of Ti from oxidized Ir/TiN also resulted in the spatially interconnected but much more nanoporous IrO_x clusters (Figures 4b, S18, and S19) than that of oxidized Ir-EG (Ir-EG after 100 h OER test at 10 mA cm^{-2}) featuring

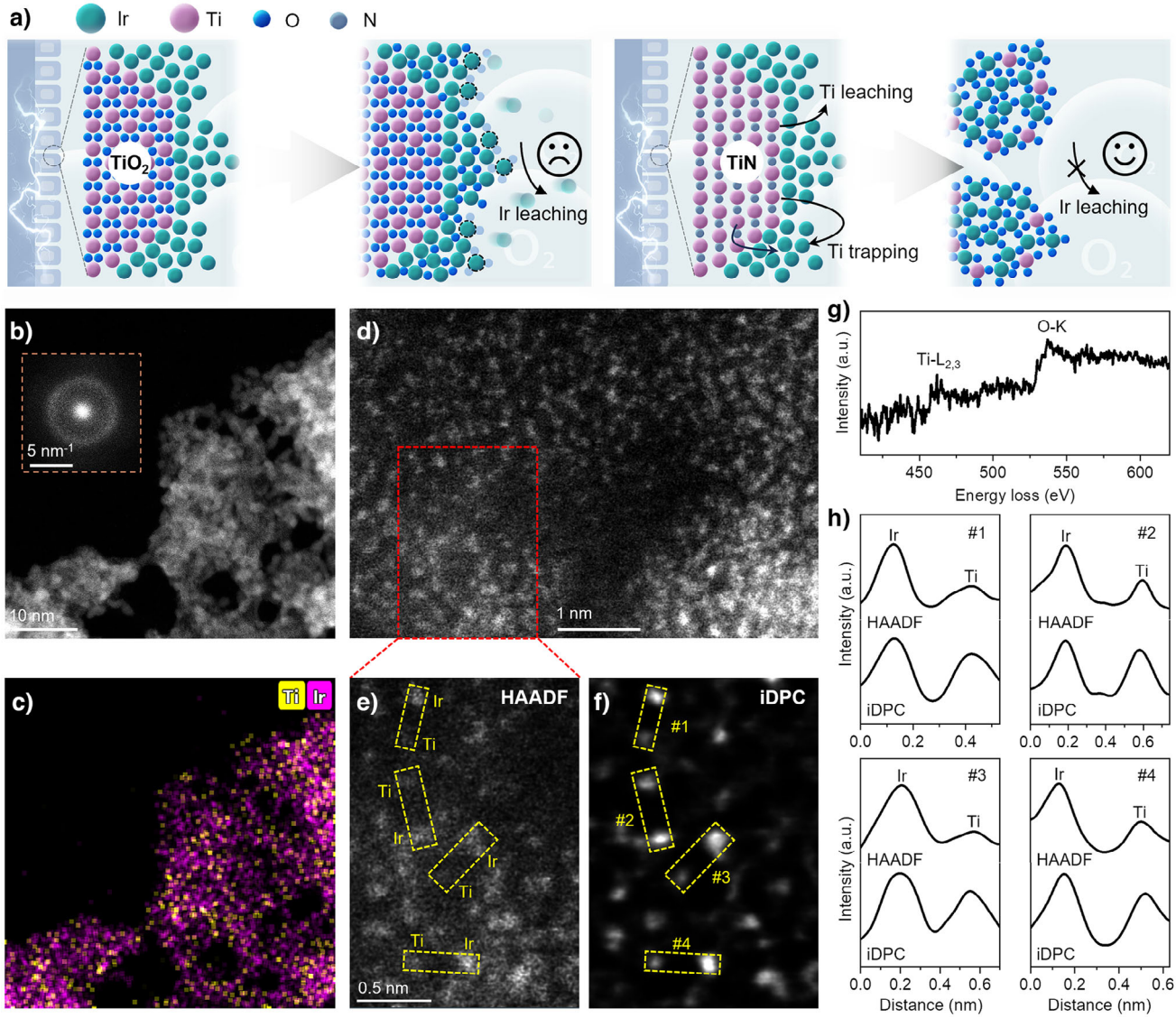

Figure 4. Atomic structure of Ti-trapped IrO_x in oxidized Ir/TiN catalyst induced by Ti leaching. a) Schematic illustration of the structural evolution for Ir/TiO_2 and Ir/TiN during OER. The conventional stable support materials like TiO_2 could hardly protect the surface Ir sites on the electrochemically oxidized amorphous IrO_x. By contrast, Ti trapping induced by TiN leaching could effectively stabilize the amorphous IrO_x against Ir leaching. b) HAADF-STEM image of Ir/TiN after 100 h test at 10 mA cm^{-2}. Inset is the corresponding FFT pattern. c) Overlap image of the Ti and Ir EDS elemental maps. d) Representative high-resolution HAADF-STEM image of oxidized Ir/TiN. e) Magnified HAADF-STEM image obtained from the area marked with red dashed rectangles in (d). f) iDPC-STEM image in the area marked with red dashed rectangles in (d). HAADF- and iDPC-STEM images were recorded simultaneously in both cases. g) EELS results of the oxidized Ir/TiN. h) Intensity profiles obtained from the areas labeled in yellow dashed rectangles in (e) and (f).

close-packed structures (Figure S20). Furthermore, the HAADF-STEM image and the corresponding EDS elemental maps (Figures 4b,c and S21) suggested that the intensive TiN leaching induced partial Ti species trapping on amorphous IrO_x clusters after prolonged OER test, which differed from the conventional understanding that the bulk TiN support could be well retained except the electrochemically formed TiO_2 passive film on the surface.[18] Such leaching-induced trapping effect was also found different from other transition metal nitride supported catalysts, e.g., Ir/NbN (Figures S22–S24). Atomic-scale structures of the oxidized Ir/TiN were further investigated via aberration-corrected scanning transmission electron microscopy (AC-STEM). In addition to HAADF-STEM imaging (Figure 4d,e), integrated differential phase contrast (iDPC)-STEM imaging (Figure 4f) was also applied to visualize the Ir (high Z number) and Ti (low Z number) atoms simultaneously as contrast in HAADF-STEM is roughly proportional to the square of the atomic number (Z^2), whereas that in iDPC-STEM is roughly linear to Z.[34] Hence, the Ir and Ti sites can be identified clearly in HAADF-STEM and iDPC-STEM, respectively, and, particularly, Ti were also confirmed by EELS (Figure 4g). As shown in the contrast analysis in Figure 4h, adjacent Ti and Ir atoms are clearly identified,

evidencing the dispersed Ti–O species trapping on amorphous IrO_x during Ti leaching from TiN support inside to outside. Inspired by the previously reported stabilized IrO_2 catalysts by atomic layer depositing TiO_2 coatings on the surface of IrO_2,[35,36] probably the significantly enhanced OER stability of Ir/TiN was contributed by the surface Ti–O species.

Given that the electrochemically oxidized iridium exhibits superior OER activity but inferior stability over the thermally oxidized ones (Figure S25), owing to the strong amorphization and the participation of activated lattice oxygen,[37–39] it will be of great importance to stabilize the iridium active sites against severe dissolution and thereby utilize its exceptional high activity.[17,40,41] For the catalysts of Ir/TiN, Ir/TiO_2, and Ir-EG, amorphization on the active Ir sites occurred when applied with OER potentials, whereas different responses of OER activity and stability were revealed. First, in situ synchrotron radiation infrared (SRIR) spectroscopy measurements were conducted to detect the evolution of oxygen-containing intermediates and explain the origin of different OER activity. As shown in Figure S26, the vibration band at ~1080 cm^{-1} emerged on Ir/TiN, Ir/TiO_2, and Ir-EG samples with the increased OER potentials, which can be assigned to the OO* intermediates.[21,22] Notably, for Ir/TiN, the OO* signals appeared at a much lower potential of 1.2 V and the intensity increased much more intensively than that of Ir/TiO_2 and Ir-EG, probably due to the weakened adsorption energy between oxygen species that contributed by the strong Ir–Ti interaction in Ir/TiN and the resulted downshift of d band center from the Fermi level.[21,22] Furthermore, in situ electrochemical impedance spectroscopy (EIS) tests (Figure S27a,b) were performed at different applied potentials (1.45–1.60 V) to detect the adsorption and desorption kinetics of the reactants on the electrode interface.[42–44] As shown in Figure S27c, the lower impedance (R_{ct}) of the OER process on oxidized Ir/TiN compared to oxidized Ir/TiO_2 at each applied potential implied the fast evolution of reactants with increased potentials. Hence, Ir/TiN exhibited much more efficient and faster four-electron-transferred OER process with higher OER performance.

Despite the composition of amorphous IrO_x in the electrochemically oxidized Ir/TiN and Ir/TiO_2, the trapping of Ti–O species on the oxidized Ir/TiN presented much more enhanced stabilization. High-resolution Ti 2p XPS spectra (Figure S28) exhibited low signals of oxidized Ir/TiN, together with a positive shift of the binding energy, further confirming that the Ti species were oxidized and very little was remained and stabilized. Ir L_3-edge XANES spectra and the corresponding second derivative curves (Figure 5a) showed lower energy of the white line position for the oxidized Ir/TiN and oxidized Ir/TiO_2 than IrO_2, indicating the existence of mixed $Ir^{3+/4+}$ species and the involvement of Ir(III) active sites toward OER in the electrochemically oxidized Ir-based samples. Moreover, the white line position of the oxidized Ir/TiN was more negative than that in oxidized Ir/TiO_2, inferring higher electronic density of Ir in oxidized Ir/TiN and thereby a higher fraction of the sustained Ir(III) sites. It is conductive to protect the highly active but unstable Ir(III) sites in the electrochemically oxidized amorphous IrO_x against overoxidation and crystallization into its less active crystalline counterpart.[45,46] The EXAFS spectra (Figure 5b) probed the elongated Ir—O bonds in oxidized Ir/TiN compared with oxidized Ir/TiO_2. It could be associated with the weakened Ir–O covalency resulted by the bonded Ti–O–Ir motifs, which makes it difficult for lattice oxygen oxidation, thereby increasing the stability of Ir active sites and prevent Ir dissolution.[47–49] The results agree well with the enhanced intrinsic activity and stability of the previously reported OER catalysts by depositing TiO_2 to tune the binding environment of surface IrO_2.[35,36,50]

Density functional theory (DFT) calculations were further conducted for atomic understanding. To explore the complex surfaces of oxidized Ir/TiN featuring Ti-trapped IrO_x, conventional possible exposed crystal facets of IrO_2 were examined to analyze as many different structural states as possible. Meanwhile, both the Ti doping and loading configurations were considered to characterize possible trapping of Ti–O species on IrO_2 surface (Figure S29). First, the influence on the Ir oxidation state was investigated according to Bader charge analysis (Figures 5c and S30a). It demonstrated that the Ti trapping would promote electron accumulation around Ir sites in IrO_2 modified with surface Ti–O species, implying the restricted overoxidation and protection of Ir(III). Such electron-enriched environment can also provide more electrons, which is beneficial to the activation of the reaction intermediates and the consequent high OER activity.[22,51,52] Furthermore, the effect of Ti trapping on the Ir–O bonding length at the catalyst surface was also explored, with average bond length used as a measure of the bonding change variation (Table S3). As shown in Figures 5d and S30b, the Ir–O bonding length increased in comparison with the catalyst without Ti introduction, where the surrounding Ti species gave a pull on the O atoms, leading to the elongated Ir—O bond and making it different for lattice oxygen oxidation. Unambiguously, the above calculation results revealed the consistent trend in line with the experimental characterizations.

Operando Raman tests were also implemented to detect the structure response of amorphous IrO_x under applied OER potentials (1.1–1.5 V). As shown in Figure 5e,f, Raman peaks at ~430 and 580 cm^{-1} appeared in both samples of oxidized Ir/TiN and oxidized Ir/TiO_2, which can be identified as γ and ε peaks of Ir–O stretching, respectively.[53] With the applied potential increased, the ε peaks of Ir–O stretching for oxidized Ir/TiN exhibited negative shifts, whereas the oxidized Ir/TiO_2 showed negligible change. According to a mathematical correlation of $\nu = 25823\exp(-1.902d)$ between metal–oxygen bond length (d) and the stretching frequencies (ν),[54] the negative shifts of the ε peaks in oxidized Ir/TiN can be related to the elongated Ir–O bonding during OER. It is consistent with the EXAFS results that oxidized Ir/TiN exhibited elongated Ir–O bonding owing to the surface Ti trapping on amorphous IrO_x, which is conductive to reducing the Ir–O covalency, thus mitigating lattice oxygen oxidation and the resulted Ir/O leaching.[50] Subsequently, online differential electrochemical mass spectroscopy (DEMS) with isotope labeling measurements were carried out to identify the involvement of lattice oxygen in OER. The pristine Ir/TiN and Ir/TiO_2 were first sufficiently electrochemically

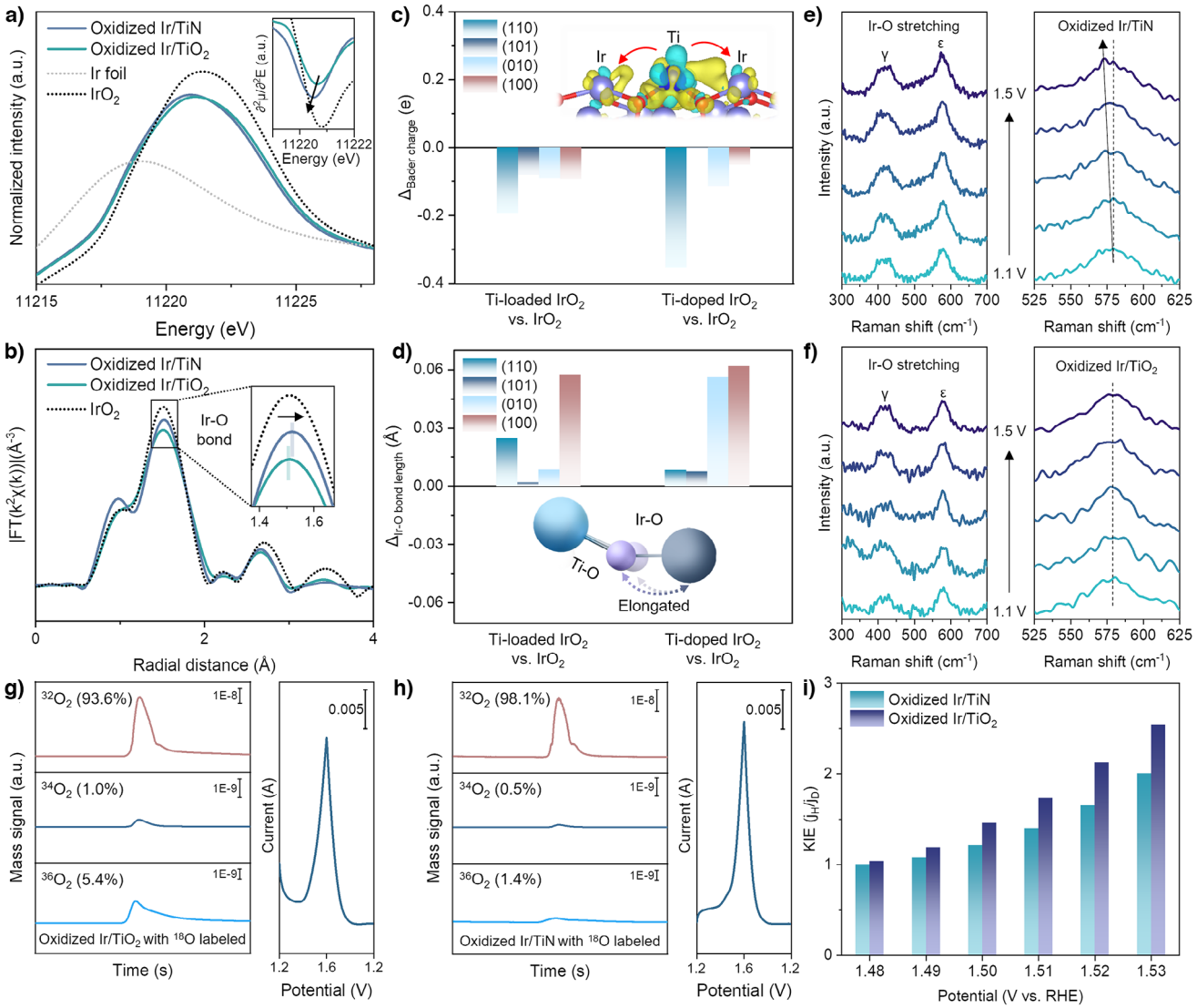

Figure 5. Mechanism of Ti trapping-stabilized amorphous IrO_x catalyst. a) Normalized Ir L_3-edge XANES spectra of oxidized Ir/TiN and oxidized Ir/TiO_2, which experienced sufficient electrochemical oxidation and surface IrO_x amorphization after 100 h OER test at 10 mA cm^{-2}. Inset shows the corresponding second derivative curves. b) Fourier-transforms of k^2-weight Ir L_3-edge EXAFS spectra of oxidized Ir/TiN and oxidized Ir/TiO_2. Calculated c) Bader charge difference and d) Ir—O bond length difference of oxidized Ir/TiN (i.e., Ti-loaded IrO_2 or Ti-doped IrO_2 models) versus pure IrO_2 model. Distinctly, both the Ti doping and loading configurations of IrO_2 with various possible crystal facets showed promoted electron accumulation around Ir sites and elongated Ir—O bond length compared with pure IrO_2, implying the restricted overoxidation of Ir(III) and the lowered Ir–O covalency that can protect the lattice oxygen from oxidation in oxidized Ir/TiN catalyst. Inset (c) is the charge density difference for Ti-trapped IrO_2, showing electron accumulation around Ir sites with surrounding trapped Ti species. Gray, indigo blue, and red balls represent Ti, Ir, and O atoms, respectively. The yellow area shows electron accumulation, whereas the blue area is meant for electron depletion. Inset (d) shows the elongated Ir—O bonds by the surrounding introduced Ti species. Operando Raman spectra of e) oxidized Ir/TiN and f) oxidized Ir/TiO_2. Raman peaks at ~430 and 580 cm^{-1} appeared in oxidized Ir/TiN, and oxidized Ir/TiO_2 can be identified as γ and ε peaks of Ir–O stretching, respectively. With the applied potential increased, the ε peaks of Ir–O stretching shifted to lower Raman shifts for oxidized Ir/TiN, whereas the oxidized Ir/TiO_2 showed negligible change. DEMS signals of $^{32}O_2$, $^{34}O_2$, and $^{36}O_2$ gas products and the corresponding CV profiles for g) ^{18}O labeled oxidized Ir/TiO_2 and h) ^{18}O labeled oxidized Ir/TiN tested in 0.5 M H_2SO_4 with $H_2{}^{16}O$ as the solvent. i) KIE values of oxidized Ir/TiN and oxidized Ir/TiO_2. It showed that the KIE values (j_H/j_D) of oxidized Ir/TiN were distinctly lower than that of oxidized Ir/TiO_2 throughout the reaction potential interval, indicating the superior proton transfer kinetics resulting from the Ti trapping on IrO_x.

oxidized at 10 mA cm^{-2} for 100 h and then labeled with ^{18}O during CV cycles in 0.5 M H_2SO_4 with $H_2{}^{18}O$ as the solvent. After thoroughly rinsed and dried, the ^{18}O-labeled catalysts were then tested in $H_2{}^{16}O$ electrolyte. The resultant $^{34}O_2$ and $^{36}O_2$ products (Figure 5g,h) containing ^{18}O lattice oxygen suggested the occurrence of lattice oxygen mechanism (LOM) on both samples. Nevertheless, the proportion of the evolved $^{34}O_2$ and $^{36}O_2$ products was distinctively diminished from 6.4% for oxidized Ir/TiO_2 to 1.9% for oxidized Ir/TiN, corresponding to 70% reduction of LOM process, which explained why the Ir leaching was remarkably reduced. Kinetic isotope effect (KIE) analyses were also carried

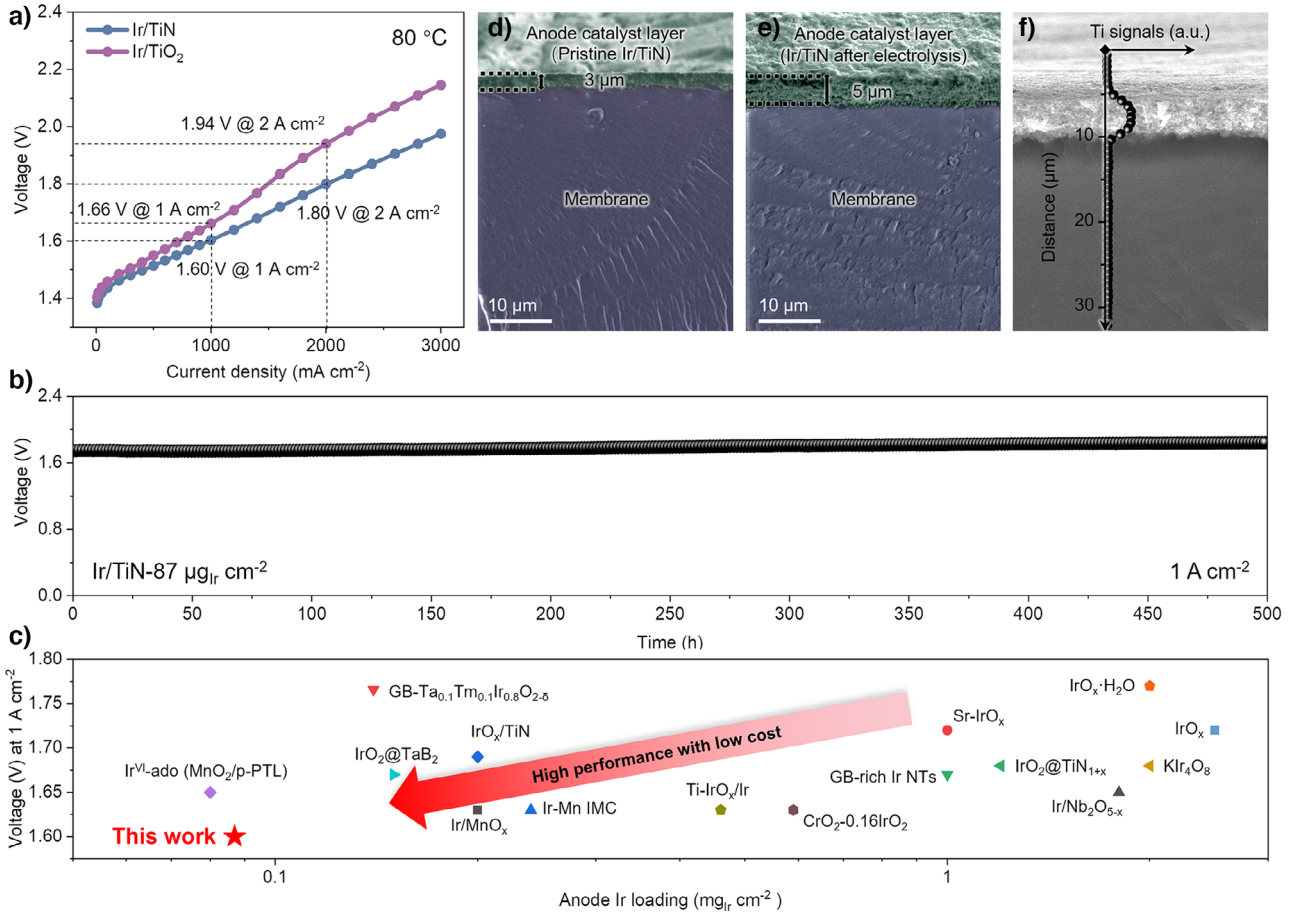

Figure 6. PEMWE performance. a) Polarization curves (without *i*R compensation) of PEMWE using Ir/TiN and Ir/TiO_2 as anode catalysts, respectively. b) Chronopotentiometry curve of the PEMWE using Ir/TiN as the anode catalyst operating at 1.0 A cm^{-2} at 80 °C and ambient pressure. c) Comparisons of the PEMWE performance with recent reported works. Detailed information is shown in Tables S4–S7. False-colored SEM images of cross-section of the CCM coated with 87 μg_{Ir} cm^{-2} Ir/TiN catalyst d) before and e) after PEMWE stability test. f) SEM image of cross-section of the CCM coated with 87 μg_{Ir} cm^{-2} Ir/TiN catalyst after PEMWE stability test and EDS line scanning near the anode catalyst layer/membrane interface, showing negligible Ti signals in the membrane and indicating there was no apparent precipitation of Ti species and the relevant structural damage to the membrane after severe Ti leaching.

out to understand the origin of efficient and robust OER performance for oxidized Ir/TiN. As is generally acknowledged, the oxygen source for acidic OER derives from multiple deprotonation process of H_2O, thereby the proton transfer properties are significant factors that affect the OER reaction rate.[55] Therefore, polarization curves (Figure S31a,b) of oxidized Ir/TiN and oxidized Ir/TiO_2 were collected in 0.5 M H_2SO_4/H_2O and 0.5 M D_2SO_4/D_2O, respectively. It showed that the KIE values (j_H/j_D) of oxidized Ir/TiN were distinctly lower than that of oxidized Ir/TiO_2 throughout the reaction potential interval (Figure 5i), indicating the superior proton transfer kinetics resulting from the Ti trapping on IrO_x. It agrees with the previously reported role of proton acceptors for the Ti–O species, accelerating deprotonation of oxo-intermediates and thus facilitating fast OER kinetics.[56] More importantly, according to the OER/dissolution cycle for iridium-based catalysts proposed by Kasian et al.,[41] the accelerated deprotonation by the trapped Ti–O species would also facilitate the OER recycle on the Ir(III) surface sites while suppressing the competing dissolving reaction, thereby reducing Ir(III) dissolution and accounting for its improved stability. In whole, these results gave insights into the significant role of TiN leaching-induced Ti trapping effect in stabilizing the active amorphous IrO_x.

PEMWE Performance

The performance of the Ir/TiN as an anode catalyst was finally evaluated in PEMWE. Catalyst coated membrane (CCM) with a 5 cm^2 working area was prepared via a decal transfer method. As analyzed by ICP-OES, the anode Ir loading for Ir/TiN catalyst was as low as 87 μg_{Ir} cm^{-2}. Despite such low Ir loading, the polarization curve of PEMWE operating at 80 °C and ambient pressure showed low cell voltages of 1.60 and 1.80 V to achieve the current density of 1.0 and 2.0 A cm^{-2}, which were much lower than those of Ir/TiO_2 (1.66 and 1.94 V at 1.0 and 2.0 A cm^{-2}, respectively) (Figure 6a). It was also competitive with the PEMWE using commercial Ir black anode (Figure S32). Furthermore, the

Ir/TiN catalyst exhibited a steady operation during 500 h stability test at 1.0 A cm^{-2} with a degradation of only 5% in the cell voltage (Figure 6b), confirming the successful stabilization of electrochemically oxidized amorphous IrO_x by Ti trapping even at practical harsh operating conditions. The PEMWE performance was also compared with those applying the advanced Ir-based anode catalysts (Figure 6c and Tables S4–S7). Impressively, the PEMWE using Ir/TiN anode catalyst exhibited a powerful competitivity in high performance together with low cost.

The cross-section and top view morphology of the CCM before and after PEMWE stability test were further compared via scanning electron microscope (SEM) to investigate the influence of TiN leaching on the electrode architecture. The pristine CCM exhibited a thickness of ~3 μm for the anode Ir/TiN catalyst layer (Figure 6d), consistent with its relatively low catalyst loading amount. Differently and impressively, it was self-thickened with the thickness increasing to ~5 μm after PEMWE test (Figure 6e), probably due to the much more nanoporous agglomerates of IrO_x clusters in oxidized Ir/TiN (Figures 4b and S18, as compared with the oxidized Ir-EG shown in Figure S20) that resulted from gradual leached TiN support, which simultaneously served as porogens. Moreover, the top view morphology of the CCM showed the Ir/TiN catalyst layers were composed of uniformly distributed particles in pristine (Figure S33a), whereas, after stability test, the TiN leaching turned the agglomerates into curly stacked ones (Figure S33b), which may also lead to self-thickened catalyst layers. As a contrast, there was no significant difference in the thickness of the Ir/TiO_2 catalyst layers before and after test (Figure S34). Voltage distribution of the PEMWE was analyzed to deduce the impact of self-thickening on the resistance during electrolysis. The voltage can be divided into kinetic overpotential ($\eta_{Kinetic}$), ohmic overpotential (η_{Ohmic}), and mass transfer overpotential ($\eta_{Mass\ transfer}$) (Figure S35). It is noteworthy that the mass transfer overpotential for Ir/TiN was effectively suppressed compared to that for Ir/TiO_2, particularly under high current densities (e.g., >2 A cm^{-2}). It may be attributed to the deduced gas transport resistance due to the formation of nanoporous catalyst layer during self-thickening process, which is essential to improve the energy efficiency of the PEMWE at high-ampere-level current densities in realistic devices. The SEM-EDS line scanning (Figure 6f) was further conducted to confirm if the membrane would be deteriorated by the severe Ti leaching. In fact, negligible Ti signals were detected within the membrane, indicating there was no apparent precipitation of Ti species and the relevant structural damage to the membrane. The findings unambiguously demonstrated its feasibility in practical application of PEMWE. It is also worth mentioning that conventional ultrathin catalyst layers would result in a series of problems such as the structural integrity, mechanical stability, in-plane electrical connectivity, and so on.[57] These issues make it infeasible to decrease Ir loading directly by lowering catalyst coating.[14] However, here the leachable TiN support induced self-thickened catalyst layers enabled the availability of ultrathin catalyst coatings without structural problems mentioned above and thereby was instructive to the future design of advanced electrode architectures for PEMWE.

Conclusion

In summary, we have demonstrated the evolution of TiN support materials at oxidative OER potentials with severe Ti leaching and elucidated that the leaching-induced Ti trapping effect stabilizes the electrochemically oxidized amorphous IrO_x. The synthesized Ir/TiN exhibits an optimal OER activity compared with Ir/TiO_2 and Ir-EG, with a mass activity 74 times higher than the commercial IrO_2/TiO_2 (Umicore). Notably, the amorphous IrO_x derived from the electrochemical oxidation of Ir/TiN shows enhanced OER stability, resulting in 84% and 89% reduction in Ir leaching compared to unsupported and TiO_2-supported counterparts. The Ir/TiN catalyst exhibits a stable operation over 1000 h at 10 mA cm^{-2} with a decay rate of only 42 μV h^{-1}. Structural characterizations together with DFT calculations reveal that the trapped Ti–O species on amorphous IrO_x mitigate the overoxidation of Ir(III) species and elongate Ir—O bonds, which contributes to 70% reduction of lattice oxygen oxidation, effectively stabilizing the amorphous IrO_x. The gradual leaching of TiN support from Ir/TiN during oxidization also results in porous interconnected IrO_x clusters, facilitating self-thickening of the catalyst layer during operation of PEMWE. This enables an ultralow Ir/TiN catalyst loading of 87 μg_{Ir} cm^{-2} for PEMWE while yielding low cell voltages of 1.60 and 1.80 V at 1.0 and 2.0 A cm^{-2}, respectively, together with a stable operation at 1.0 A cm^{-2} for 500 h. Our findings deepen the understanding of the structure–performance relationships of nonoxide support materials for OER catalysts and pave a way toward the future design of advanced electrode architectures with ultrathin catalyst layer and thereby lowering Ir loading for PEMWE.

Supporting Information

The authors have cited additional references within Supporting Information.[41,58–62]

Acknowledgements

This work was financially supported by the National Natural Science Foundation of China (22239001, 51920105003, 22376062, and 22379043), the Shanghai Pilot Program for Basic Research (22TQ1400100-12), the Science and Technology Commission of Shanghai Municipality (23520710700 and 22ZR1415700), and the Fundamental Research Funds for the Central Universities. The authors thank the Frontiers Science Center for Materiobiology and Dynamic Chemistry and National Synchrotron Radiation Laboratory (NSRL). The authors also thank the Shanghai Synchrotron Radiation Facility of BL14B1 (https://cstr.cn/31124.02.SSRF.BL 14W1) for the assistance on XAFS measurements and the 1W1B-XAFS Beamline of Beijing Synchrotron Radiation Facility (https://cstr.cn/31109.02.BSRF. 1W1B) for providing technical support and assistance in XAFS data collection. The authors also thank Shanghai Aitins Technology Co., Ltd. for their support and assistance in first-principles calculations.

Conflict of Interests

The authors declare no conflict of interest.

Data Availability Statement

The data that support the findings of this study are available from the corresponding author upon reasonable request.

Keywords: Amorphous catalysts · Metal nitrides · Oxygen evolution reaction · Proton exchange membrane water electrolysis · Stabilization

[1] R. Ram, L. Xia, H. Benzidi, A. Guha, V. Golovanova, A. Garzón Manjón, D. Llorens Rauret, P. Sanz Berman, M. Dimitropoulos, B. Mundet, E. Pastor, V. Celorrio, C. A. Mesa, A. M. Das, A. Pinilla-Sánchez, S. Giménez, J. Arbiol, N. López, F. P. García de Arquer, *Science* **2024**, *384*, 1373–1380.
[2] A. Li, S. Kong, K. Adachi, H. Ooka, K. Fushimi, Q. Jiang, H. Ofuchi, S. Hamamoto, M. Oura, K. Higashi, T. Kaneko, T. Uruga, N. Kawamura, D. Hashizume, R. Nakamura, *Science* **2024**, *384*, 666–670.
[3] P. De Luna, C. Hahn, D. Higgins, S. A. Jaffer, T. F. Jaramillo, E. H. Sargent, *Science* **2019**, *364*, eaav3506.
[4] H. N. Nong, L. J. Falling, A. Bergmann, M. Klingenhof, H. P. Tran, C. Spori, R. Mom, J. Timoshenko, G. Zichittella, A. Knop-Gericke, S. Piccinin, J. Perez-Ramirez, B. R. Cuenya, R. Schlogl, P. Strasser, D. Teschner, T. E. Jones, *Nature* **2020**, *587*, 408–413.
[5] W.-X. Zheng, X.-X. Cheng, P.-P. Chen, L.-L. Wang, Y. Duan, G.-J. Feng, X.-R. Wang, J.-J. Li, C. Zhang, Z.-Y. Yu, T.-B. Lu, *Nat. Commun.* **2025**, *16*, 337.
[6] J. Kibsgaard, I. Chorkendorff, *Nat. Energy* **2019**, *4*, 430–433.
[7] M. A. Hubert, L. A. King, T. F. Jaramillo, *ACS Energy Lett.* **2022**, *7*, 17–23.
[8] M. Faustini, M. Giraud, D. Jones, J. Rozière, M. Dupont, T. R. Porter, S. Nowak, M. Bahri, O. Ersen, C. Sanchez, C. Boissière, C. Tard, J. Peron, *Adv. Energy Mater.* **2019**, *9*, 1802136.
[9] L. Tao, F. Lv, D. W. Wang, H. Luo, F. X. Lin, H. Y. Gong, H. T. Mi, S. G. Wang, Q. H. Zhang, L. Gu, M. C. Luo, S. J. Guo, *Joule* **2024**, *8*, 450–460.
[10] Z. Xie, X. Liang, Z. Kang, Y. Zou, X. Wang, Y. A. Wu, G. King, Q. Liu, Y. Huang, X. Zhao, H. Chen, X. Zou, *CCS Chem.* **2025**, *7*, 216–228.
[11] D. Hoffmeister, S. Finger, L. Fiedler, T. C. Ma, A. Körner, M. Zlatar, B. Fritsch, K. W. Bodnar, S. Carl, A. Götz, B. A. Zubiri, J. Will, E. Spiecker, S. Cherevko, A. T. S. Freiberg, K. J. J. Mayrhofer, S. Thiele, A. Hutzler, C. van Pham, *Adv. Sci.* **2024**, *11*, 2402991.
[12] Y. Wang, Z. Zhao, X. Liang, X. Zhao, X. Wang, S. Jana, Y. A. Wu, Y. Zou, L. Li, H. Chen, X. Zou, *Adv. Mater.* **2024**, *36*, 2407717.
[13] S. Ge, R. Xie, B. Huang, Z. Zhang, H. Liu, X. Kang, S. Hu, S. Li, Y. Luo, Q. Yu, J. Wang, G. Chai, L. Guan, H.-M. Cheng, B. Liu, *Energy Environ. Sci.* **2023**, *16*, 3734–3742.
[14] M. Bernt, A. Siebel, H. A. Gasteiger, *J. Electrochem. Soc.* **2018**, *165*, F305–F314.
[15] Y. Chen, H. Li, J. Wang, Y. Du, S. Xi, Y. Sun, M. Sherburne, J. W. Ager, 3rd, A. C. Fisher, Z. J. Xu, *Nat. Commun.* **2019**, *10*, 572.
[16] H. Luo, F. Lin, Q. Zhang, D. Wang, K. Wang, L. Gu, M. Luo, F. Lv, S. Guo, *J. Am. Chem. Soc.* **2024**, *146*, 19327–19336.
[17] S. Geiger, O. Kasian, M. Ledendecker, E. Pizzutilo, A. M. Mingers, W. T. Fu, O. Diaz-Morales, Z. Li, T. Oellers, L. Fruchter, A. Ludwig, K. J. J. Mayrhofer, M. T. M. Koper, S. Cherevko, *Nat. Catal.* **2018**, *1*, 508–515.
[18] S. Zaman, M. Khalid, S. Shahgaldi, *ACS Energy Lett.* **2024**, *9*, 2922–2935.
[19] R. Zeng, H. Li, Z. Shi, L. Xu, J. Meng, W. Xu, H. Wang, Q. Li, C. J. Pollock, T. Lian, M. Mavrikakis, D. A. Muller, H. D. Abruña, *Nat. Mater.* **2024**, *23*, 1695–1703.
[20] Y. Yuan, J. Wang, S. Adimi, H. Shen, T. Thomas, R. Ma, J. P. Attfield, M. Yang, *Nat. Mater.* **2020**, *19*, 282–286.
[21] X. Han, T. Mou, A. Islam, S. Kang, Q. Chang, Z. Xie, X. Zhao, K. Sasaki, J. A. Rodriguez, P. Liu, J. G. Chen, *J. Am. Chem. Soc.* **2024**, *146*, 16499–16510.
[22] G. Li, K. Li, L. Yang, J. Chang, R. Ma, Z. Wu, J. Ge, C. Liu, W. Xing, *ACS Appl. Mater. Inter.* **2018**, *10*, 38117–38124.
[23] S. Wang, H. Lv, S. Bi, T. Li, Y. Sun, W. Ji, C. Feng, C. Zhang, *Mater. Chem. Front.* **2021**, *5*, 8047–8055.
[24] G. Wang, W. Wan, M. Chen, J. Li, X. Wu, S. Huang, K. Li, X. Tian, Z. Kang, *Int. J. Hydrogen Energy* **2024**, *71*, 804–810.
[25] J. Zhao, R. Urrego-Ortiz, N. Liao, F. Calle-Vallejo, J. Luo, *Nat. Commun.* **2024**, *15*, 6391.
[26] A. Seifitokaldani, O. Savadogo, *Electrochim. Acta* **2015**, *167*, 237–245.
[27] H. Y. Lin, Z. X. Lou, Y. L. Ding, X. X. Li, F. X. Mao, H. Y. Yuan, P. F. Liu, H. G. Yang, *Small Methods* **2022**, *6*, e2201130.
[28] F. de la Peña, M. H. Berger, J. F. Hochepied, F. Dynys, O. Stephan, M. Walls, *Ultramicroscopy* **2011**, *111*, 169–176.
[29] B. Cao, K. Suenaga, T. Okazaki, H. Shinohara, *J. Phys. Chem. B* **2002**, *106*, 9295–9298.
[30] X. Zhang, C. Yang, C. Gong, M. Liu, W. Zhou, H. Su, F. Yu, F. Hu, Q. Liu, S. Wei, *Angew. Chem. Int. Ed.* **2023**, *62*, e202308082.
[31] J. Ruiz Esquius, D. J. Morgan, G. Algara Siller, D. Gianolio, M. Aramini, L. Lahn, O. Kasian, S. A. Kondrat, R. Schlögl, G. J. Hutchings, R. Arrigo, S. J. Freakley, *J. Am. Chem. Soc.* **2023**, *145*, 6398–6409.
[32] Z. Xia, H. Zhang, K. Shen, Y. Qu, Z. Jiang, *Phys. B Condens. Matter* **2018**, *542*, 12–19.
[33] J. Y. Xiaobo Zheng, P. Li, Q. Wang, J. Wu, E. Zhang, S. Chen, Z. Zhuang, W. Lai, S. Dou, W. Sun, D. Wang, Y. Li, *Sci. Adv.* **2023**, *9*, eadi8025.
[34] E. Yücelen, I. Lazić, E. G. T. Bosch, *Sci. Rep.* **2018**, *8*, 2676.
[35] C. E. Finke, S. T. Omelchenko, J. T. Jasper, M. F. Lichterman, C. G. Read, N. S. Lewis, M. R. Hoffmann, *Energy Environ. Sci.* **2019**, *12*, 358–365.
[36] R. A. Krivina, M. Zlatar, T. N. Stovall, G. A. Lindquist, D. Escalera-López, A. K. Cook, J. E. Hutchison, S. Cherevko, S. W. Boettcher, *ACS Catal.* **2023**, *13*, 902–915.
[37] L. Ouattara, S. Fierro, O. Frey, M. Koudelka, C. Comninellis, *J. Appl. Electrochem.* **2009**, *39*, 1361–1367.
[38] H. N. Nong, T. Reier, H.-S. Oh, M. Gliech, P. Paciok, T. H. T. Vu, D. Teschner, M. Heggen, V. Petkov, R. Schlögl, T. Jones, P. Strasser, *Nat. Catal.* **2018**, *1*, 841–851.
[39] C. Spöri, P. Briois, H. N. Nong, T. Reier, A. Billard, S. Kühl, D. Teschner, P. Strasser, *ACS Catal.* **2019**, *9*, 6653–6663.
[40] A. Lončar, D. Escalera-López, S. Cherevko, N. Hodnik, *Angew. Chem. Int. Ed.* **2022**, *61*, e202114437.
[41] O. Kasian, J. P. Grote, S. Geiger, S. Cherevko, K. J. J. Mayrhofer, *Angew. Chem. Int. Ed.* **2018**, *57*, 2488–2491.
[42] H. Su, W. Zhou, W. Zhou, Y. Li, L. Zheng, H. Zhang, M. Liu, X. Zhang, X. Sun, Y. Xu, F. Hu, J. Zhang, T. Hu, Q. Liu, S. Wei, *Nat. Commun.* **2021**, *12*, 6118.
[43] Y. Duan, L. L. Wang, W. X. Zheng, X. L. Zhang, X. R. Wang, G. J. Feng, Z. Y. Yu, T. B. Lu, *Angew. Chem. Int. Ed.* **2024**, *63*, e202413653.
[44] H. Y. Lin, Q. Q. Yang, M. Y. Lin, H. G. Xu, X. Tang, H. Q. Fu, H. Wu, M. Zhu, L. Zhou, H. Y. Yuan, S. Dai, P. F. Liu, H. G. Yang, *Adv. Mater.* **2024**, *36*, 2408045.

[45] G. R. Lee, J. Kim, D. Hong, Y. J. Kim, H. Jang, H. J. Han, C.-K. Hwang, D. Kim, J. Y. Kim, Y. S. Jung, *Nat. Commun.* **2023**, *14*, 5402.
[46] V. A. Saveleva, L. Wang, O. Kasian, M. Batuk, J. Hadermann, J. J. Gallet, F. Bournel, N. Alonso-Vante, G. Ozouf, C. Beauger, K. J. J. Mayrhofer, S. Cherevko, A. S. Gago, K. A. Friedrich, S. Zafeiratos, E. R. Savinova, *ACS Catal.* **2020**, *10*, 2508–2516.
[47] L. Zu, X. Qian, S. Zhao, Q. Liang, Y. E. Chen, M. Liu, B. J. Su, K. H. Wu, L. Qu, L. Duan, H. Zhan, J. Y. Zhang, C. Li, W. Li, J. Y. Juang, J. Zhu, D. Li, A. Yu, D. Zhao, *J. Am. Chem. Soc.* **2022**, *144*, 2208–2217.
[48] D. A. Kuznetsov, M. A. Naeem, P. V. Kumar, P. M. Abdala, A. Fedorov, C. R. Muller, *J. Am. Chem. Soc.* **2020**, *142*, 7883–7888.
[49] Z. Shi, Y. Wang, J. Li, X. Wang, Y. Wang, Y. Li, W. Xu, Z. Jiang, C. Liu, W. Xing, J. Ge, *Joule* **2021**, *5*, 2164–2176.
[50] Y. Wang, R. Ma, Z. Shi, H. Wu, S. Hou, Y. Wang, C. Liu, J. Ge, W. Xing, *Chem* **2023**, *9*, 2931–2942.
[51] S. Zhao, S.-F. Hung, L. Deng, W.-J. Zeng, T. Xiao, S. Li, C.-H. Kuo, H.-Y. Chen, F. Hu, S. Peng, *Nat. Commun.* **2024**, *15*, 2728.
[52] Y. Shi, J. Bai, A. Ma, Z. Zou, Y. Liu, H. Lin, D. Chen, R. Zhang, J. Lai, L. Wang, *Chem. Eng. J.* **2024**, *498*, 155834.
[53] Z. Pavlovic, C. Ranjan, Q. Gao, M. van Gastel, R. Schlögl, *ACS Catal.* **2016**, *6*, 8098–8105.
[54] F. D. Hardcastle, I. E. Wachs, *J. Raman Spectrosc.* **1995**, *26*, 397–405.
[55] J. Huang, H. Sheng, R. D. Ross, J. Han, X. Wang, B. Song, S. Jin, *Nat. Commun.* **2021**, *12*, 3036.
[56] W. Hu, B. Huang, M. Sun, J. Du, Y. Hai, W. Yin, X. Wang, W. Gao, C. Zhao, Y. Yue, Z. Li, C. Li, *Adv. Mater.* **2025**, *37*, 2411709.
[57] Y. Shi, C. Ding, Z. Lu, L. Shen, K. Huang, C. Zhao, H. Tan, C.-F. Yan, *ACS Sustain. Chem. Eng.* **2024**, *12*, 423–432.
[58] S. Niu, S. Li, Y. Du, X. Han, P. Xu, *ACS Energy Lett.* **2020**, *5*, 1083–1087.
[59] G. Kresse, D. Joubert, *Phys. Rev. B* **1999**, *59*, 1758–1775.
[60] J. P. Perdew, K. Burke, M. Ernzerhof, *Phys. Rev. Lett.* **1996**, *77*, 3865–3868.
[61] S. Grimme, *J. Comput. Chem.* **2006**, *27*, 1787–1799.
[62] Y.-R. Zheng, J. Vernieres, Z. Wang, K. Zhang, D. Hochfilzer, K. Krempl, T.-W. Liao, F. Presel, T. Altantzis, J. Fatermans, S. B. Scott, N. M. Secher, C. Moon, P. Liu, S. Bals, S. Van Aert, A. Cao, M. Anand, J. K. Nørskov, J. Kibsgaard, I. Chorkendorff, *Nat. Energy* **2021**, *7*, 55–64.

Manuscript received: February 20, 2025
Revised manuscript received: April 03, 2025
Accepted manuscript online: April 21, 2025
Version of record online: April 27, 2025